Solid Earth

Open Access

Phase change in subducted lithosphere, impulse, and quantizing Earth surface deformations

C. O. Bowin[1], W. Yi[2], R. D. Rosson[3], and S. T. Bolmer[1]

[1]Woods Hole Oceanographic Institution, Woods Hole, MA, USA
[2]Intelligenet Solutions Group, John Deere, Kaiserslautern, Germany
[3]Applications Engineering Group, MathWorks, Natick, MA, USA

Correspondence to: C. O. Bowin (cbowin@whoi.edu)

Abstract. The new paradigm of plate tectonics began in 1960 with Harry H. Hess's 1960 realization that new ocean floor was being created today and is not everywhere of Precambrian age as previously thought. In the following decades an unprecedented coming together of bathymetric, topographic, magnetic, gravity, seismicity, seismic profiling data occurred, all supporting and building upon the concept of plate tectonics. Most investigators accepted the premise that there was no net torque amongst the plates. Bowin (2010) demonstrated that plates accelerated and decelerated at rates 10^{-8} times smaller than plate velocities, and that globally angular momentum is conserved by plate tectonic motions, but few appeared to note its existence.

Here we first summarize how we separate where different mass sources may lie within the Earth and how we can estimate their mass. The Earth's greatest mass anomalies arise from topography of the boundary between the metallic nickel–iron core and the silicate mantle that dominate the Earth's spherical harmonic degree 2 and 3 potential field coefficients, and overwhelm all other internal mass anomalies. The mass anomalies due to phase changes in olivine and pyroxene in subducted lithosphere are hidden within the spherical harmonic degree 4–10 packet, and are an order of magnitude smaller than those from the core–mantle boundary. Then we explore the geometry of the Emperor and Hawaiian seamount chains and the 60° bend between them that aids in documenting the slow acceleration during both the Pacific Plate's northward motion that formed the Emperor seamount chain and its westward motion that formed the Hawaiian seamount chain, but it decelerated at the time of the bend (46 Myr). Although the 60° change in direction of the Pacific Plate at of the bend, there appears to have been nary a pause in a passive spreading history for the North Atlantic Plate, for example. This, too, supports phase change being the single driver for plate tectonics and conservation of angular momentum. Since mountain building we now know results from changes in momentum, we have calculated an experimental deformation index value (1–1000) based on a world topographic grid at 5 arcmin spacing and displayed those results for viewing.

1 Introduction

Gravity, the weakest force in our universe, has also provided us with one of the hidden keys for understanding plate tectonics. We say "hidden" because the deep positive mass anomalies within the Earth that drive the motions of the planet's tectonic plates are an order of magnitude smaller than, and hence obcured by, the Earth's greatest mass anomalies (see Fig. 5). Those greatest mass anomalies are of 0.4–3.5×10^{23} kg, which we, as Bowin (2000), interpreted as due to topography at the core–mantle boundary (CBM) at 2900 km depth. The density contrast at the core–mantle boundary, with nickel iron of the core below and silicates of the lower mantle above, is approximately 4.3 gm/cc. Thus mass anomalies due to topography of up to 3 km relief there overwhelm all other mass anomaly contributions within the Earth. The power spectrum for the gravitational field of the Earth (see Fig. 1) shows a marked break in slope between degree 3 and degree 4. A global map view of the geoid anomalies (gravitational potential field) contained in the spherical
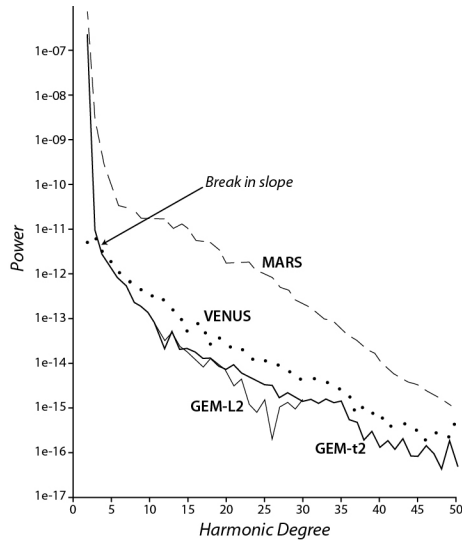
Figure 1. Power spectra for Earth, Venus, and Mars from sets of spherical harmonic coefficients. Earth (solid line) is from GEM-L2 (Lerch et al., 1982) and GEM-t2 (Marsh et al., 1990), Venus (dotted line) is from Nerem et al. (1993), and Mars (dashed line) is from Smith et al. (1993). If the horizontal harmonic degree axis were plotted as a log scale, then the spectra would be nearly a straight line.

harmonic coefficients of the Goddard Earth Model (GEM) t2 set of coefficients is shown in Fig. 2. That view of the gravitational potential field of the Earth has been a puzzle since it was first observed because it shows no correlation with surface continents nor topography, with the single exception of a positive geoid anomaly over the Andes of South America (SA). In Fig. 2 note the prominent negative geoid low in the Indian Ocean, the Sri Lanka (SL) Low, and the positive geoid, the New Guinea High (NG). And then in Fig. 3, note that the large summed contributions of degrees 2 and 3 are restricted to only those two NG and SL geoid anomaly sites. In Fig. 3, one can also see that the individual degree contributions become decreasingly smaller above degree 10. Thus, we now approach the Earth's second-largest mass anomaly as it remains buried within the spherical harmonic degree 4–10 packet. Besides illustrating the spatial distribution of the degree 4–10 geoid anomalies, Fig. 4 further demonstrates how the large contributions from the degree 2–3 dominate the 2–10, 2–30, and 2–250 geoid (seen in Fig. 2) fields. Further, Fig. 4 also visually introduces the use of vertical derivatives of the Earth's potential field into our discussion for resolving Earth structures. In the gravity degree 2–3 map note the paucity of contour lines compared to those in the degree 2–3 geoid map. Geoid anomalies ($1\,d^{-1}$) are most diagnostic of large mass anomalies at depths of thousands of kilometers, whereas gravity anomalies ($1\,d^{-2}$) are most sensitive to mass anomalies within 100 km of the surface.
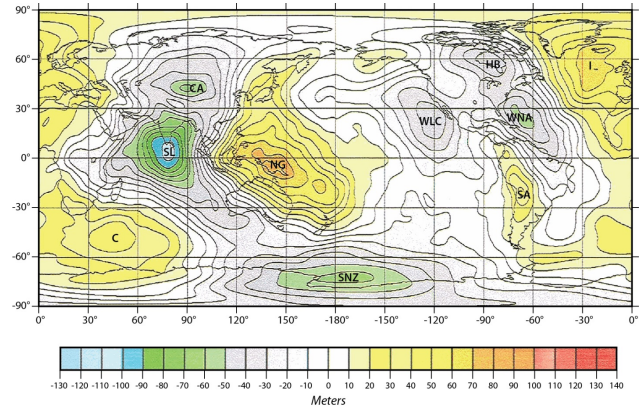

Figure 2. Earth's geoid anomaly map for spherical harmonic degree ranges 2–250. Computed Goddard Earth Model GEM-t2 coefficients (Marsh et al., 1990) are referenced to ellipsoid with reciprocal flattening of 298.257 (actual Earth flattening).
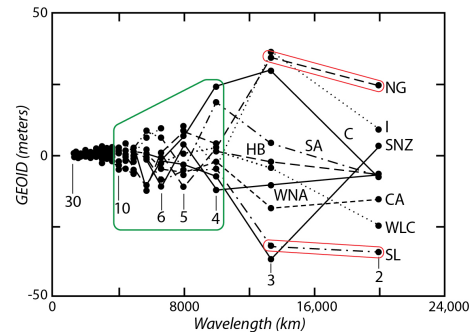

Figure 3. Magnitudes of individual harmonic degree contributions for the Earth's 10 major geoid anomaly values computed from the GEM-9 coefficients referenced with reciprocal flattening of 298.257 (actual Earth flattening). Four positive anomalies are New Guinea (NG), Iceland (I), Crozet (C), and South America (SA). Six negative anomalies are Indian Ocean (Sri Lanka) (SL), west of lower California (WLC), central Asia (CA), and south of New Zealand (SNZ). Reprinted from Bowin (1985) with permission.

Consider a site directly over a point mass, the geoid anomaly (N) is

$$N = \frac{V}{g_0} = \frac{GM}{g_0^2},$$

where V is the disturbing potential, g_0 is normal gravity ($9.8\,\mathrm{m\,s^{-2}}$), G is the gravitational constant, M is the anomalous mass, and z is the depth of the point mass. The vertical component of gravity g due to the same point mass is

$$g = \frac{GM}{Z^2}.$$

The ratio of gravity anomaly to the geoid anomaly directly above the point mass at depth z is then
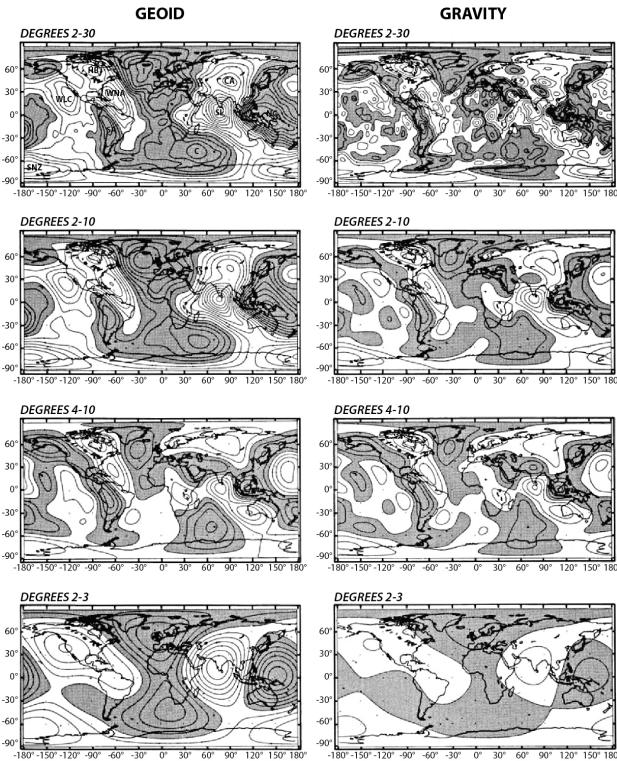
$$\frac{g}{N} = \frac{g_0}{z}.$$

Figure 4. Geoid and gravity anomaly maps from GEM-L2 spherical harmonic coefficients. Referenced to ellipsoid with reciprocal flattening of 298.257 (actual Earth flattening). Contour intervals are 10 m and 20 mGal, respectively. Degree 2–30 maps obtained by summing contributions from degrees 2 through 30. Degree 2–10, 4–10, and 2–3 maps similarly obtained. In the geoid degree 2–30 map (and in Fig. 2) the 10 major anomalies are labeled, and identified in Fig. 3.

Conversely, the depth can be determined by

$$Z = \frac{g_0}{g/N}.$$

Then, of course, reentering the value of z into either, or both, of the point-mass equations for the geoid or gravity can provide estimates of the causative mass. It was by this means that the magnitudes of the mass anomalies of the Earth shown in Fig. 5 were estimated. Two additional vertical derivatives of the gravity potential can also aid in defining shallower mass anomaly structures: the vertical gravity gradient ($1 d^{-3}$) and the vertical gradient of the vertical gravity gradient ($1 d^{-4}$).

For each mass element within the Earth, its geoid contribution falls off as $1 d^{-1}$ with distance, gravity as $1 d^{-2}$, vertical gravity gradient $1 d^{-3}$, and vertical gravity gradient of vertical gravity gradient $1 d^{-4}$. But because all masses within the Earth contribute to all harmonic degrees, it is impossible to invert any one field into its causative masses. However, at selective locations the ratio of gravity anomaly divided by the geoid anomaly value at center locations (Fig. 5) has
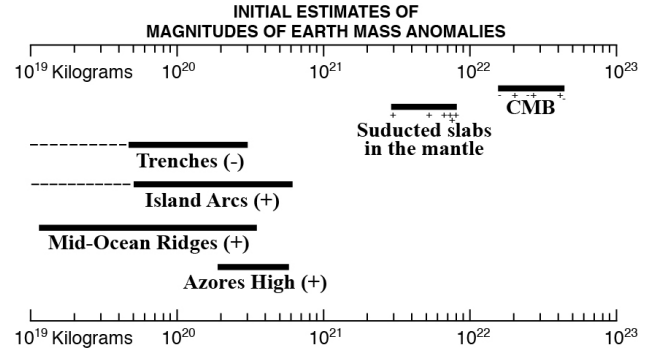

Figure 5. Initial estimates of the magnitudes of Earth mass anomalies. Estimates are calculated from ratios of gravity anomaly divided by geoid anomaly values at anomaly centers.

already provided constraints on the internal mass anomaly structure of the Earth (Bowin, 1983, 1986, 1991, 2000). At lithospheric subduction sites (positive geoid anomaly band in degree 4–10 map in Fig. 4), the phase changes of olivine and pyroxene grains in the subducted lithosphere are inferred to produce the positive density contrast with the surrounding upper mantle, which forms the second-greatest mass anomalies within the Earth ($2.0 - 8 \times 10^{22}$ kg).

For many decades there has been agreement that viscous flow within the mantle could theoretically lead to topographic and mass perturbations at the Earth's surface and at density horizons at depth (Pekeris, 1935; Hager, 1984). As the blog "Retos Terricolas" (5 June 2014), "Dynamic topography vs. isostasy: The importance of definitions", nicely points out, dynamic topography was originally coined by oceanographers Bruce (1968) and Wyrtki (1975) to refer to deviations of the ocean surface relative to the geoid after subtracting effects due to tides, waves, and wind by time filtering. The remaining deviations of "dynamic topography" related to water currents in the oceans are the oceanographers goal. In the 1980s the term dynamic topography was adopted by solid-Earth scientists but included "static" forces, such as the weight of sinking plates. Hager and O'Connell (1981), Hager et al. (1985), and Ricard et al. (1993) inferred a triplet of mass anomalies by adding negative downward deflections of the ocean surface and at the core–mantle boundary below due to mantle flow. In this scenario the positive mass of the sinking slab would become masked by both of those two dynamic flow-induced negative depressions. For a mass at a single depth, to be the source for a geoid anomaly would require all of its vertical derivatives to have the same equivalent point-mass depths. To utilize that fact for a test, Bowin (1994, 2000) computed spherical harmonic coefficients from balanced sets at six different depths (100, 500, 1000, 2000, 2900, 4000 km). This was done for balanced sets of two positive and two negative masses and another balanced set of three positive and three negative masses to provide for both even- and odd-order harmonic values. By then
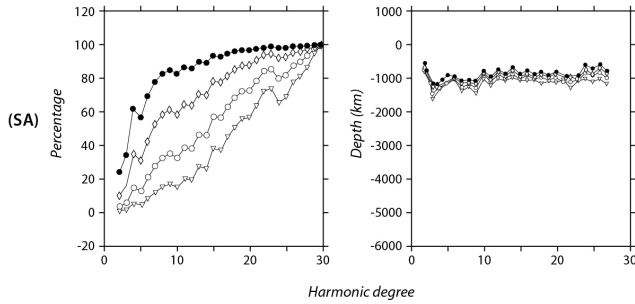
Figure 6. Percentage contribution curve (CCC) and estimated equivalent point-mass depths for the South American (SA) GEM-t2 geoid high. Depths are estimated from the percentage CCC using spline function coefficients for each degree. Spline functions are from model sets of two and three balanced point masses at depths of 100, 500, 1000, 2900, and 4000 km.

calculating and displaying calculated cumulative contribution curves (CCC) (see, e.g., Bowin (2000), Fig. 12) plotted as percentages of their maximum value, estimates of depths to point-mass sources could be estimated for each potential derivative. The result for the SA geoid high shown in Fig. 6 yielded a consistent point-mass depth of nearly 1200 km depth for all harmonic degrees and all derivatives, indicating a single source as its origin and hence a shallower depth for the actual positive mass anomaly. This 1200 km point-mass depth is also consistent with the SA geoid high source being shallower above the zero contour line at 2900 km depth of the core–mantle topography (Fig. 4, degree 2–3 geoid). This strong evidence for a single source depth for the South American geoid high is strong support opposing dynamic topography as being a significant contributor to the Earth's geoid.

2   Deriving high derivative Earth potential field model

The gravity field coefficients are estimated with high accuracy in the long-wavelength part (corresponding to the coefficients of low degrees). In order to avoid filtering these low degree coefficients, we shift the damping factors above to a certain degree (30) and obtain a new set of filtered coefficients that have yielded stable estimates of global geoid, gravity, vertical gravity gradient, and vertical gradient of vertical gravity gradient anomaly values for degrees 31–264. These coefficients reflect mass anomalies that exist in the outer 200 km of the Earth. Our derived filtered spherical harmonic coefficients for degrees 2–264 are given in the accompanying Supplement.

Various alternative methods exist for the determination of global gravity field models – such as integration on Earth sphere, least-square adjustment or collocation – and various data sources are used, such as satellite-based data or terrestrial (surface) observations. The error behaviors of the resulting gravity field models depend on the method, the quality and properties of the observations. In general, the

gravity field is not homogeneously determined. With satellite gravimetry the high-frequency part (corresponding to the gravity field coefficients of higher degrees) is computed less accurately than the low-frequency part. This results in some short-wavelength noise in the computed gravity field models. It is therefore necessary to apply filtering to extract the signal by suppressing the accompanying noise.

The idea of filtering gravity field models in the spectral domain is based on smooth SH coefficients with some depression factors. Various smooth functions have been proposed such as Pellinen (1966) and Jekeli (1981). With a Gaussian mean filter in the spectral domain as an example, as presented by Jekeli (1981), the recursive formula for a Gaussian smoothing coefficients in the spectral domain is given as

$$\beta_0 = 1,$$

$$\beta_1 = \frac{1 + e^{-2b}}{1 - e^{-2b}} - \frac{1}{b},$$

$$\beta_n = \frac{-2n + 3}{b}\beta_{n-1} + \beta_{n-2}, \quad n \geq 3,$$

where $b = \frac{\ln 2}{1 - \cos(r/R_\oplus)}$ with r the radius of a spherical cap to be smoothed and $R_\oplus$ the radius of the Earth.

Using the above filter coefficients, the filtered gravity field coefficients can be derived as

$$\begin{Bmatrix} \overline{C'}_{nm} \\ \overline{S'}_{nm} \end{Bmatrix} = \beta_n \begin{Bmatrix} \overline{C}_{nm} \\ \overline{S}_{nm} \end{Bmatrix}.$$

The gravity field coefficients are estimated with high accuracy in the long-wavelength part (corresponding to the coefficients of low degrees). In order to avoid filtering these low degree coefficients, we shift the damping factors above to a certain degree n_0 and obtain a new set of filter coefficients such that

$$\beta'_n = 1, \quad n < n_0$$
$$\beta'_n = \beta_{n-n_0}, \quad n \geq n_0.$$

The gravity field coefficients are estimated with high accuracy in the long-wavelength part (corresponding to the coefficients of low degrees). In order to avoid filtering these low degree coefficients, we shift the damping factors above to a certain degree (30) and obtain a new set of filter coefficients that have yielded stable estimates of global geoid, gravity, vertical gravity gradient, and vertical gradient of vertical gravity gradient anomaly values for degrees 31–264. These coefficients reflect mass anomalies that exist in the outer 200 km of the Earth.

Plots of our results are shown in Fig. 7 for degree 31–264 contributions for geoid, gravity, vertical gravity gradient, and vertical gradient of vertical gravity gradient together all demonstrate that the only principle mass anomalies in the outer 200 km of the Earth are those of the negative mass anomalies associated with fore-arc lithosphere depressions, and the positive mass anomalies of the uplifted island arc/mountain ranges.
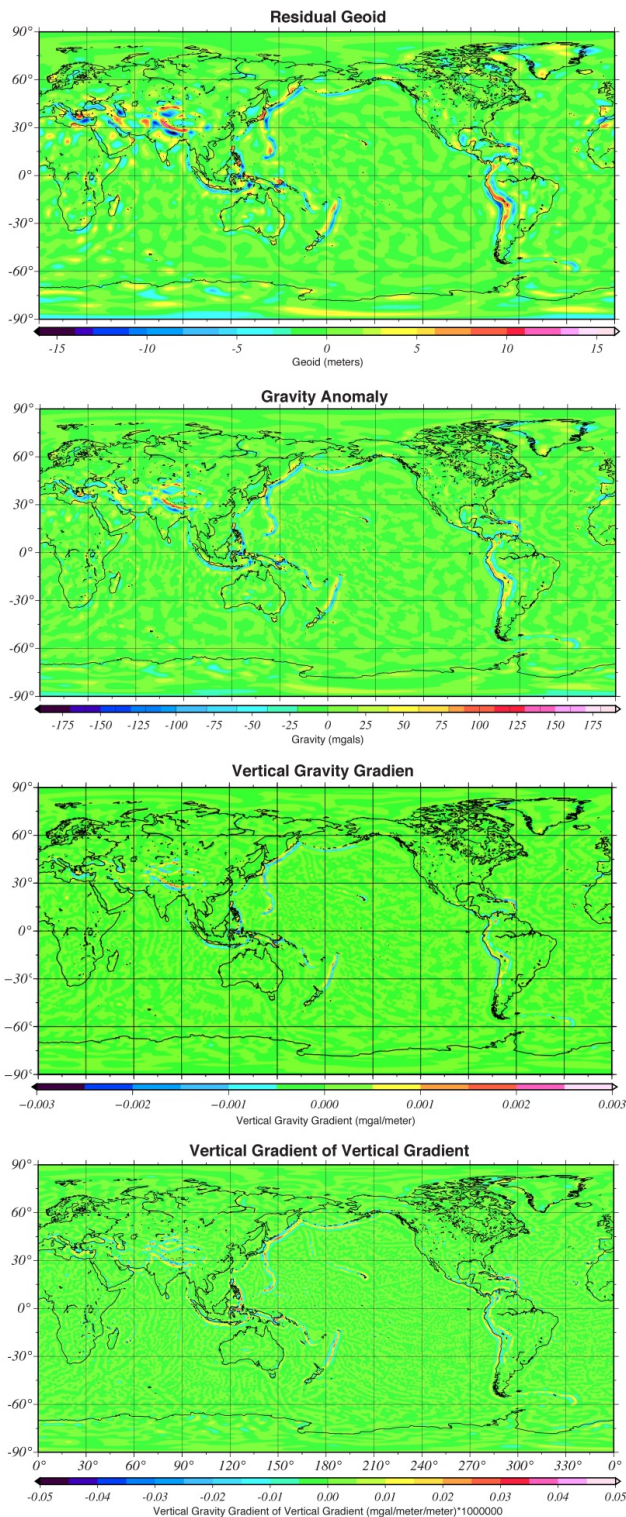
Figure 7. Residual geoid, gravity, vertical gravity gradient, and vertical gradient of vertical gravity gradient for spherical harmonic degrees 31–464. Color scale weighted so that each color has same number of data samples.

3 Motions of the Earth's tectonic plates and earthquakes

In 1960 Harry H. Hess was the first to recognize that the ocean floor was not everywhere ancient (Precambrian) but is, in fact, locally, being created today (Hess, 1960; it was to be published in "The Sea, Ideas and Observations" but became delayed). Robert S. Dietz received a copy of the Hess (1960) preprint and published a paper, Dietz (1961), on seafloor spreading without acknowledging Hess's prior work. Dietz concluded that ocean basins most likely contained rocks no older than the Mesozoic, and he also noted that linear magnetic anomalies aligned normal to the presumed flow direction of the presumed convection cells were being found in the Atlantic. Hess then had his paper published in the next available Geological Society of America (GSA) publication volume available, Hess (1962). Magnetic anomaly stripes were reported in the Atlantic Ocean by Vine and Mathews (1963). Wilson (1963) in his Fig. 4 referenced forming the Hawaiian chain over a "stable core of a convection cell" as a possible origin of the Hawaiian chain of islands, whose source later was identified as being to hot spot plumes. Looking back with hindsight, we see a remarkable coming-together of oceanic magnetic anomaly stripes that allowed linkage to normal and reverse paleomagnetic age dating of the oceanic crust beneath, as well as the global patterns of rifts and transform faults. And, in turn, aided in the dating of folded and deformed rocks of the former or active subduction collision zones, the depressed sections at rifts, and the horizontal displacements along strike-slip faults, like that of the San Andreas, all fit into the new understanding of plate tectonics and its three types of boundaries. Another consequence of plates rubbing against one another while moving is to increase strains in the rocks of the opposing plates, which, when released, cause an earthquake. In this way, the distribution of epicenters reveals the locations of plates and their boundaries, as in Fig. 8. However, that figure only displays those having earthquakes having a magnitude 6 or greater; hence the less seismically active borders do not stand out.

Essentially all the analyses of plate motions (Morgan, 1973; Soloman and Sleep, 1974; Forsyth and Uyeda, 1975; Chapple and Tullis, 1977) have assumed that plates are not undergoing acceleration. Accordingly, every plate must be in dynamic equilibrium, such that the sum of the torques about any axis must be zero. Previously, the paucity of clear evidence for systematic plate velocity changes through time has led researchers to view convective motion in the mantle, with traction on the overlying lithosphere, as likely producing plate tectonics, in which plates would move in stages with a terminal velocity. Different stages might have different plate motion direction and/or speed.

Harada and Hamano (2000) made a simple but profound assumption: that hot spots on the Pacific (PA) Plate were "fixed" in time and space relative to each other. With
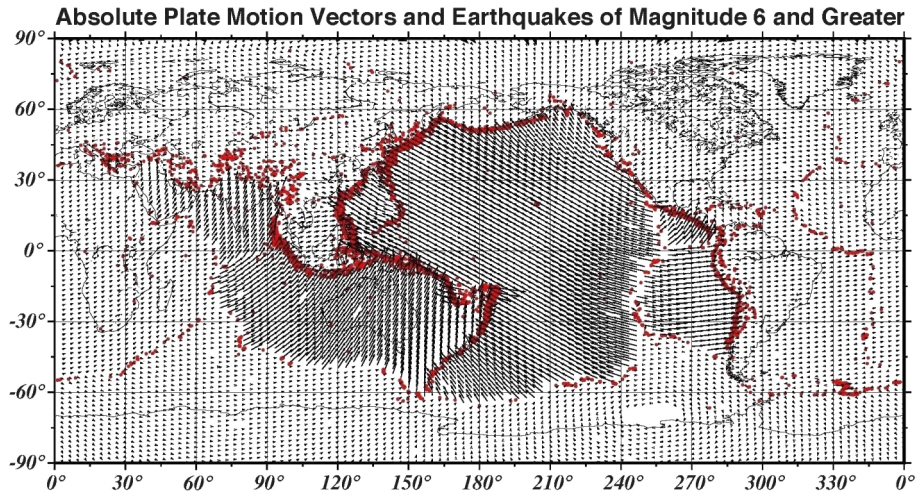
Figure 8. Absolute plate velocity vectors (1 per 1000 plotted black arrows) for the 52 plates of Bird (2003) and earthquake locations with magnitudes greater than magnitude 6.0.

that assumption, they formed a spherical triangle amongst the center points of the Hawaiian, Louisville, and Easter Island hotspots. This triangle was then used to identify which digitized location points along the Emperor–Hawaiian seamount chain correlated with which digitized points along the Louisville ridge chain. Then, with those location points correlated in time, they could begin estimating poles of rotation. They then took each location point along the Emperor–Hawaiian chain, and bisected its arc with the Hawaii hotspot location and at that bisect point projected a line normal to it. They then did the same procedure to the equivalent point along the Louisville chain with its bend, and where the two normal lines intersect is an equivalent stage pole for that selected point. From ages of dredged samples, they estimated Euler poles at 4 and 2 Myr intervals. Figure 9, from Bowin and Kuiper (2005) using the Harada and Hamano (2000) Euler poles, had the Pacific Plate speeding up as it moved northward toward the Aleutians, then after the bend slowed down, and then again increased speed as it moved towards the Marianas (away from Hawaii).

Bowin (2010) demonstrated that plate tectonics conserves angular momentum (see Fig. 10) using the 14-major-tectonic-plate history of the Earth (except the Juan de Fuca and Philippine plates). Euler stage pole histories of the past 62 million years of Gripp and Gordon (1990) were given. We believe it is worth restating that "mirroring of the bend in the Emperor–Hawaiian seamount chain in the locations of the 4448 filtered stage pole locations for the absolute motions of the Nazca Plate (Bowin, 2010; Plate No. 11, Fig. 12) gives credence to both the quaternion analyses utilized and the role of impulse in plate motions". Of the 14 plates analyzed, the Nazca Plate is the only one that has a stage pole pattern revealing such a pronounced bend in stage pole trend at 46 Myr.

For this present study of active surface deformation we have chosen to use a more detailed 52 tectonic plate model of the Earth's surface by Bird (2000). Bird's published Euler pole values are relative to a fixed Pacific Plate. An important contribution was provided by Rick Rosson (Table 1) of Math-works.com, who converted Bird's 52 relative Euler poles to absolute poles of rotation (Table 1)

Although the rates of plate acceleration/deceleration are very small, they are real and thus indicate that impulse (force times time) due to changes in plate momentums (plate mass times velocity) are what causes deformations within the Earth and on its surface. Thus one of our early tasks was to display the individual plate motion absolute velocity vectors for the 52 plates utilizing the absolute rotation Euler pole data of Table 1 on a global rectangular grid having 5 arcmin spacing (see Fig. 8).

Earthquakes occur as a result from the release of strain that accumulates in the Earth, and those strains, in turn, result from plate motions. Therefore, this dependency proves that the maximum energy for seismicity is similarly bounded. Thus, we contend that this new knowledge of plate acceleration/deceleration opens a new portal through which earthquakes and lithospheric strain accumulation must now be viewed. We can now state that there will never be a magnitude 12 earthquake. We can also confidently state that there will never be a magnitude 11 earthquake. We cannot rule out the possibility that earthquakes of a very low magnitude 10 might occur. This is because the seismicity time constant for strain build-up in the crust is on the order of thousands of years, and we only have barely a century of seismicity observations. Furthermore, at the present GPS receiver sensitivities, nearly 100 years of GPS observations are required to directly assess present-day plate acceleration.

Table 1. Euler pole and angular velocity estimates; based on Pacific Plate absolute rotation from Morgan and Morgan (2007).

		Relative to PA						Absolute					
		Euler pole degrees		Angular velocity degrees per million years				Euler pole degrees		Angular velocity degrees per million years			
ID	Plate	Latitude	Longitude	Magnitude	Direction			Latitude	Longitude	Magnitude	Direction		
					X	Y	Z				X	Y	Z
1	AF	59.160	−73.174	0.927	0.148	−0.491	0.859	43.068	−24.555	0.154	0.664	−0.304	0.683
2	AM	57.645	−83.736	0.931	0.058	−0.532	0.845	47.023	−77.471	0.131	0.148	−0.665	0.732
3	AN	64.315	−83.084	0.870	0.052	−0.430	0.901	69.152	72.937	0.100	0.104	0.340	0.935
4	AP	33.639	−81.177	0.916	0.128	−0.823	0.554	−27.269	−76.653	0.400	0.205	−0.865	−0.458
5	AR	59.658	−33.193	1.162	0.423	−0.277	0.863	33.902	10.771	0.559	0.815	0.155	0.558
6	AS	74.275	−87.237	0.650	0.013	−0.271	0.963	−15.574	96.510	0.243	−0.109	0.957	−0.268
7	AT	56.283	8.932	1.640	0.548	0.086	0.832	33.335	32.439	1.226	0.705	0.448	0.550
8	AU	69.080	1.742	1.074	0.357	0.011	0.934	29.853	50.295	0.629	0.554	0.667	0.498
9	BH	12.559	87.957	0.303	0.035	0.975	0.217	−41.586	91.990	0.941	−0.026	0.748	−0.664
10	BR	45.900	−111.000	0.200	−0.249	−0.650	0.718	−62.004	106.970	0.619	−0.137	0.449	−0.883
11	BS	16.007	122.442	2.125	−0.516	0.811	0.276	−2.480	117.942	2.415	−0.468	0.883	−0.043
12	BU	8.894	−75.511	2.667	0.247	−0.957	0.155	−7.103	−73.760	2.249	0.278	−0.953	−0.124
13	CA	54.313	−79.431	0.904	0.107	−0.573	0.812	19.074	−60.781	0.134	0.461	−0.825	0.327
14	CL	10.130	−45.570	0.309	0.689	−0.703	0.176	−67.700	46.992	0.688	0.259	0.277	−0.925
15	CO	36.823	−108.629	1.998	−0.256	−0.759	0.599	22.317	−116.239	1.334	−0.409	−0.830	0.380
16	CR	−12.628	175.127	3.605	−0.972	0.083	−0.219	−22.274	168.708	3.901	−0.907	0.181	−0.379
17	EA	28.300	66.400	11.400	0.352	0.807	0.474	24.386	67.477	11.418	0.349	0.841	0.413
18	EU	61.066	−85.819	0.859	0.035	−0.483	0.875	82.549	−125.636	0.062	−0.076	−0.105	0.992
19	FT	−10.158	−178.305	4.848	−0.984	−0.029	−0.176	−17.805	176.821	5.054	−0.951	0.053	−0.306
20	GP	9.799	79.690	5.275	0.176	0.970	0.170	2.122	80.790	5.598	0.160	0.986	0.037
21	IN	60.494	−30.403	1.103	0.425	−0.249	0.870	30.740	17.045	0.528	0.822	0.252	0.511
22	JF	35.000	26.000	0.507	0.736	0.359	0.574	−30.453	60.181	0.789	0.429	0.748	−0.507
23	JZ	35.910	70.166	22.520	0.275	0.762	0.587	33.923	70.693	22.430	0.274	0.783	0.558
24	KE	47.521	−3.115	2.831	0.674	−0.037	0.738	36.355	9.218	2.357	0.795	0.129	0.593
25	MA	43.777	149.205	1.278	−0.620	0.370	0.692	9.106	133.230	1.224	−0.676	0.719	0.158
26	MN	−3.037	150.456	51.300	−0.869	0.492	−0.053	−3.789	150.080	51.573	−0.865	0.498	−0.066
27	MO	59.589	78.880	0.893	0.098	0.497	0.862	5.316	86.493	0.857	0.061	0.994	0.093
28	MS	11.103	−56.746	4.070	0.538	−0.821	0.193	1.468	−53.682	3.640	0.592	−0.805	0.026
29	NA	48.709	−78.167	0.749	0.135	−0.646	0.751	−51.875	−48.699	0.163	0.407	−0.464	−0.787
30	NB	−4.000	139.000	0.330	−0.753	0.654	−0.070	−46.155	114.429	0.989	−0.286	0.631	−0.721
31	ND	58.664	−89.003	0.701	0.009	−0.520	0.854	−60.423	123.324	0.106	−0.271	0.412	−0.870
32	NH	13.000	−12.000	2.700	0.953	−0.203	0.225	−1.873	−3.134	2.543	0.998	−0.055	−0.033
33	NI	6.868	−168.868	3.255	−0.974	−0.192	0.120	−5.356	−176.147	3.227	−0.993	−0.067	−0.093
34	NZ	55.578	−90.096	1.360	−0.001	−0.565	0.825	49.949	−95.741	0.563	−0.064	−0.640	0.765
35	OK	55.421	−82.859	0.845	0.071	−0.563	0.823	4.138	−70.042	0.072	0.340	−0.937	0.072
36	ON	48.351	142.415	2.853	−0.527	0.405	0.747	33.309	134.502	2.625	−0.586	0.596	0.549
37	PA	0.000	0.000	0.000	1.000	0.000	0.000	−59.330	94.900	0.803	−0.044	0.508	−0.860
38	PM	54.058	−90.347	0.907	−0.004	−0.587	0.810	18.588	−107.084	0.137	−0.278	−0.906	0.319
39	PS	−1.200	−45.800	1.000	0.697	−0.717	−0.021	−44.243	−25.003	1.020	0.649	−0.303	−0.698
40	RI	36.700	−105.200	4.692	−0.210	−0.774	0.598	32.016	−107.586	3.987	−0.256	−0.808	0.530
41	SA	54.999	−85.752	0.636	0.042	−0.572	0.819	−75.217	100.241	0.175	−0.045	0.251	−0.967
42	SB	10.610	−32.990	8.440	0.824	−0.535	0.184	6.122	−30.689	8.097	0.855	−0.507	0.107
43	SC	48.625	−81.454	0.652	0.098	−0.654	0.750	−80.395	−31.677	0.204	0.142	−0.088	−0.986
44	SL	63.121	−97.084	0.856	−0.056	−0.449	0.892	40.224	163.787	0.113	−0.733	0.213	0.646
45	SO	58.789	−81.637	0.978	0.075	−0.513	0.855	55.293	−67.498	0.178	0.218	−0.526	0.822
46	SS	19.529	135.017	1.478	−0.667	0.666	0.334	−6.491	126.226	1.738	−0.587	0.802	−0.113
47	SU	55.447	−72.955	1.103	0.166	−0.542	0.824	42.103	−52.024	0.325	0.457	−0.585	0.670
48	SW	−19.019	−39.640	1.840	0.728	−0.603	−0.326	−41.053	−28.277	1.964	0.664	−0.357	−0.657
49	TI	19.524	112.175	1.514	−0.356	0.873	0.334	−5.783	108.348	1.831	−0.313	0.944	−0.101
50	TO	28.807	2.263	9.300	0.876	0.035	0.482	24.970	5.143	8.980	0.903	0.081	0.422
51	WL	22.134	132.330	1.546	−0.624	0.685	0.377	−3.483	124.268	1.778	−0.562	0.825	−0.061
52	YA	69.067	−97.718	0.998	−0.048	−0.354	0.934	67.697	146.639	0.261	−0.317	0.209	0.925

4 What is going on inside the Earth?

Bowin (2010) demonstrated that it is the sinking of the positive phase change mass anomalies of the subducted lithosphere that drive plate tectonics. The present locations of those positive mass anomalies are most clearly revealed in the spherical harmonic degree 4–10 coefficient packet of the Earth's potential field. As the linear bands of subducted litho-sphere gradually shift locations, so, too, will the degree 4–10 and order coefficients change that delineate their location pattern within the degree 4–10 packet. Indeed, many questions of Earth history could be better answered if we knew how the Earth's past potential coefficients differed from today's. But, alas, we do not and cannot. According to classical geodesy we have to assume that the absolute motion of the Pacific Plate at any time results from instantaneous in-
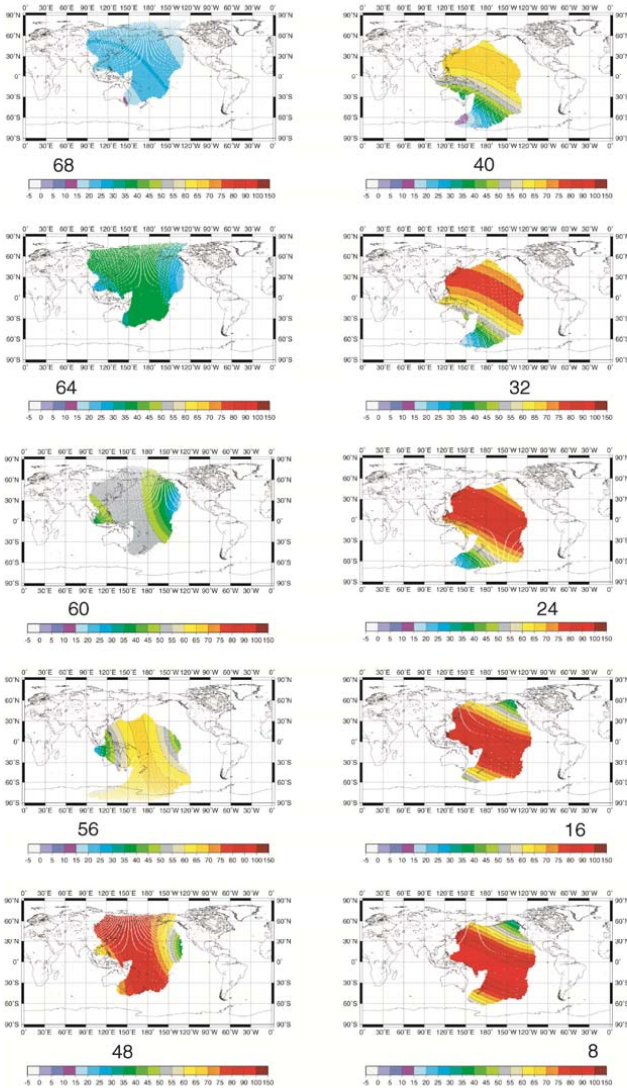
Emperor Hawaiian

Figure 9. Stage pole velocities for Pacific Plate at labeled time on Emperor and Hawaiian seamount chains. From Bowin and Kuiper (2005).
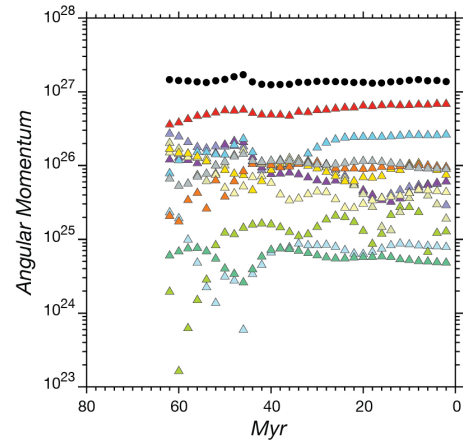
Angular Momentum – 4448

Figure 10. Angular momentum vs. Myr for 4448 individual filtered plate data over 62–0 Myr of Bowin (2010) and their sum (black circles). Plate ID for plates: AF (Africa, dark grey), AN (Antarctica, dark blue), CA (Caribbean, dark green), CO (Cocos, yellow green), EN (Eurasia, light yellow), IN (India, pale yellow), NA (North America, dark yellow), NZ (Nazca, orange), PA (Pacific, red), and SA (South America, light grey).

Figure 8 provides a present-day sample of how the Earth is behaving after its motion changed from the Emperor seamount chain northward mantle motion era to the Hawaiian seamount construction era of westward mantle motion. In particular, note that the absolute easterly motion of the direction of the Pacific Plate, from the north end of the Tonga trench to the south end of the Yap trench, is essentially at 90° to the northerly motion of the adjacent Australian (Au) Plate to the south. An inability to satisfactorily visualize the interface between a northern down-going subduction limb of an Australian thermal convection roller cell and a side-slipping transcurrent portion of a Pacific roller thermal-driven convection cell led Bowin (2010) to reject that scenario as not being credible. And bear in mind that this geometric setting would have persisted for more than 40 Myr.

Whereas Fig. 8 illustrates the absolute vector motions of the present 52 plates, Fig. 11 summarizes the global patterns of oceanic linear magnetic anomalies and transform faults, and thereby records a history of past events. Particularly striking is the apparent consistency shown by the magnetic record for the separation of North and South America from Africa with the opening of the Atlantic Ocean since the Middle Jurassic. This matching of the coastlines was noted in the initial ideas of continental drift by Wegener (1912). The bold-labeled numbers (2, 2a, 2b, 3a, 3b, 4a, 4b, 4c, 5) illustrate the migration progression of a pattern of plate propagation extended south from the South Pacific, separating Australia from Antarctica and continuing westward across the Indian Ocean into the Gulf of Aden and then up the Red Sea to the Gulf of Aqaba (Bowin, 1974). It was not until
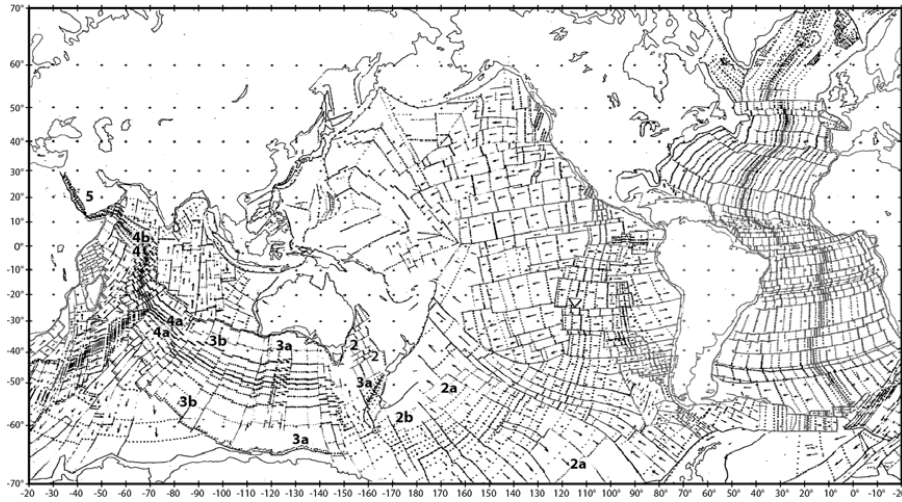
tegration of responses to all internal Earth mass anomalies. However, Fig. 10 suggests that other plates may vary their momentums more rapidly than this Pacific Plate example. Although the resultant momentum Pacific Plate vectors remained near constant but had different rates for tens of millions of years during the Emperor and Hawaiian seamount times, the direction changed azimuth by 60° within about 4 million years.

Figure 11. Mercator map of oceanic magnetic anomalies and transform faults. Scanned copy of the original 1986 illustration.
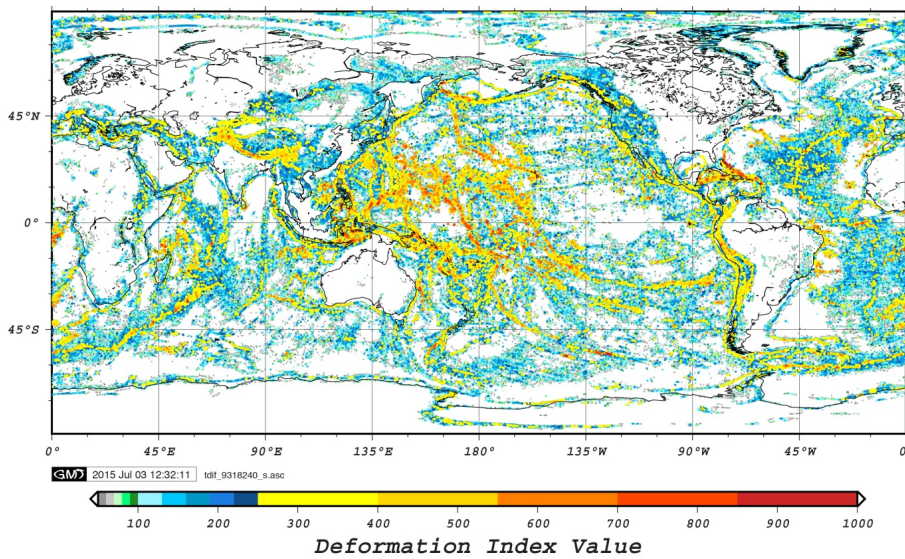

Figure 12. World view of deformation index value (1–1000) based on a global topographic grid at 5 arcmin spacing. At each grid location, the maximum relief in meters of the location with the eight adjacent surrounding locations is divided by 5 to obtain its deformation index value.

nearly 36 years later that Bowin (2010) recognized that that beginning of that extension of the South Pacific spreading into the Indian Ocean realm began at the time of the bend in the Emperor–Hawaiian seamount chain (46 Myr). And it appears to have begun with the wedge-shaped opening (spreading) of the Tasman Sea off eastern Australia (labeled 2). Then the Pacific Plate spreading progressed southward (2a, 2b), to progressing westward, separating Australia from Antarctica (3a, 3b), and continuing through time to progress westward, moving India northward towards Eurasia, and then opening the Gulf of Aden and hence the Red Sea, to now the Gulf of Aqaba. A southwest-trending branch of a closely spaced young pattern of spreading and transform offsets can also be seen emanating from the triple-junction point in the Indian Ocean east of Madagascar. This branch coincides with that classified as ultraslow-spreading ocean ridges (Dick et al., 2003).

The remnant of a former Mesozoic triple junction remains evident in the magnetic anomaly pattern in the western Pacific Ocean basins (Fig. 9). In the eastern portion of the central and North Pacific Ocean basin, note the appearance of several south–north-trending propagations of axes of spreading there, with some dominating over a former trend. Besides the fact that the magnetic age reversal timescale has given us an extremely valuable record into past events, our brief overview of oceanic magnetic anomaly patterns has demon-
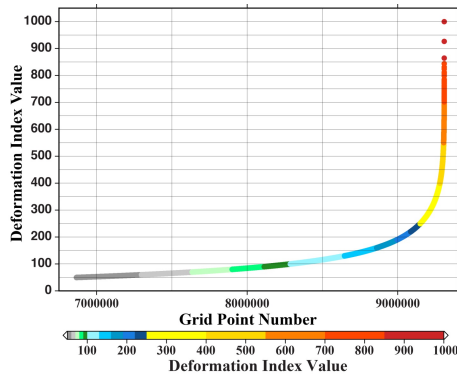
Figure 13. Deformation index values sorted lowest to greatest value vs. sort point number. Note that more than the first 6 million values have values less than 50, and that accounts for the white areas in Fig. 12.

strated that plate tectonic motions are not chaotic. The motions seem rather slow and steady. Even the 60° change in azimuth of lithosphere flow that accompanied the "bend" in the Emperor–Hawaiian seamount chain trend near 46 Myr appeared to have not affected the spreading in the Atlantic Ocean, although it did coincide with the beginning of a significant rearrangement of continents in the Southern Hemisphere. The band of positive geoid anomalies in the degree 4–10 packet (Fig. 4, degrees 4–10) shows good agreement with the absolute plate motion vectors for present-day plate motions (Fig. 8), supporting the phase-change conclusion of Bowin (2010). Unfortunately, we cannot satisfactorily estimate what the Earth's spherical harmonic degree 4–10 coefficients were for the time period before the bend (say, 90–50 Kyr). Without such a quantitative understanding of a period before the bend with a period after the bend, the best estimates of rates of Earth's internal mass redistributions will remain those of Fig. 4.

We have now become forced to assume the Earth's spherical harmonic coefficients for degrees 4–10 must change with time to meet the evolving location pattern of dense phase-change subducted lithosphere and periodotic material. Perhaps one should consider that the coefficients for harmonic degrees 2–3 may also evolve with time, and that the locations of the Indian Low (Sri Lanka Low) and New Guinea High locations may also shift with time. But it it appears to be only the smaller mass anomalies of the falling dense masses of the phase change mass anomalies that conserve the angular momentum of the global plate tectonic system. The unanswered question now shifts to the following: how does such a planetary system of conservation of angular momentum become activated?

5   Quantifying a deformation index value

Since we can now view "mountain building" deformation as resulting from changes of momentum or impulse, how might such deformations be quantized? Topographic perturbations from a global mean value are a first-order measure of a degree of uplift or subsidence that has occurred in a region, but we sought a deformation index value that would be more relevant than simply a local topographic mean or standard deviation or a combination value. Our selection for this initial test of a deformation index value is to use, at each 5 arcmin pixel, the maximum absolute topographic difference with its eight adjacent neighboring pixels. We used this as a way to estimate the absolute maximum local topographic relief value at each grid location as a stand-in for a deformation index value.

Figure 12 presents our first global view of approximately 9 million maximum topographic relief values at 5 arcmin spacing using a color scale where the topographic relief in meters is divided by 5 so that the resulting deformation index value lies between 1 and 1000. Here, in addition to the orange and reds associated with the mountainous belts of the Himalayan and Andean ranges, and island arcs of the world, they also locate many of the undersea rises of the southwest Indian Ocean, western Pacific Ocean, and North and South Atlantic mid-ocean rises. And in the northwestern Pacific Ocean basin, a series of non-red nearly east–west-trending, quasi-equally spaced fracture zone features stand out. We are also struck (and puzzled) by the great abundance of yellow and orange colors from topographic relief in the western central Pacific region. It stands out as a unique part of the world. If deformation index values less than 50 are ignored, and those above 50 are sorted from lowest to highest, then a plot like Fig. 13 results. Figure 13 also helps clarify that over 6 million grid locations in the world map of Fig. 12 have deformation index values of less than 50 and hence are white on that map.

The Supplement related to this article is available online at doi:10.5194/se-6-1075-2015-supplement.

Edited by: J. C. Afonso

References

Bird, P.: An updated digital model of plate boundaries, Geochem. Geophy. Geosy., 4, 1027, 2003.

Bowin, C.: Depth of principal mass anomalies contributing to the Earth's geoidal undulations and gravity anomalies, Mar. Geod., 7, 61–100, 1983.

Bowin, C.: Global gravity maps and the structure of the Earth, in: The Utility of Regional Gravity and Magnetic Anomaly Maps, edited by: Hinze, W. J., 88–101, Soc. Of Explor. Geophys., Tulsa, OK, USA, 1985.

Bowin, C.: Topography at the core-mantle boundary, Geophys. Res. Lett., 13, 1513–1516, 1986.

Bowin, C.: Earth's Gravity Field and Plate Tectonics, Tectonophysics issue with contributions to Texas A&M Geodynamics Silver Anniversary Symposium, 187, 69–89, 1991.

Bowin, C.: The geoid and deep Earth mass anomaly structure, in: Geoid and Its Geophysical Interpretations, edited by: Vanicek, P. and Christou, N. T., 343 pp., CRC Press, Boca Raton, FL, USA, 1994.

Bowin, C.: Mass anomaly structure of the Earth, Rev. Geophys., 38, 355–387, 2000.

Bowin, C.: Plate tectonics conserves angular momentum, eEarth, 5, 1–20, doi:10.5194/ee-5-1-2010, 2010.

Bowin, C. and Kuiper, H.: Resolving accelerations of Earth's Plate tectonics, Poster at AGU Meeting Toronto, Canada, Abstract No. #T43C-01, available at: ftp://ftp.whoi.edu/pub/users/cbowin, 2005.

Bruce, J. G.: Comparison of near surface dynamic topography during the two monsoons in the western Indian Ocean. Deep Sea Research and Oceanographic Abstracts, Vol. 15, No. 6, Elsevier, Princeton, NJ, USA, 1968.

Chapple, W. M. and Tullis, T. E.: Evaluation of the forces that drive the plates, J. Geophys. Res., 82, 1967–1984, 1977.

Dick, H. J. B., Lin, J., and Schoouten, H.: An ultraslow-spreading class of ocean ridge, Nature, 246, 405–412, 2003.

Dietz, R. S.: Continental and Ocean Basin Evolution by Spreading of the Sea Floor, Nature, 190, 854–857, 1961.

Forsyth, D. and Uyeda, S.: On the relative importance of the driving forces of plate motion, Geophys. J. Roy. Astr. S., 43, 163–200, 1975.

Gripp, A. E. and Gordon, R. R. G.: Current plate velocities relative to the hotspots incorporating the NUVEL-1 global plate motion model, Geophys. Res. Lett. 17, 1109–1112, 1990.

Hager, B. H.: Subducted slabs and the geoid: Constraints on mantle rheology and flow, J. Geophys. Res., 89, 6003–6015, 1984.

Hager, B. H. and R. J. O'Connell: A simple global model of plate dynamics and mantle convection, J. Geophys. Res., 86, 4843–4867, 1981.

Hager, B. H., Clayton, R. W., Richards, M. A., Comer, R. P., and Dziewonski, A. M.: Lower mantle heterogeneity, dynamic topography, and the geoid, Nature, 313, 541–545, 1985.

Harada, Y. and Hamano, Y.: Recent progress on the plate motion relative to hotspots, in: The History and Dynamics of Global Plate Motions, Geoph. Monog. Series., 121, 327–338, 2000.

Hess, H. H.: Preprint Evolution Ocean Basins, Princeton Univ. Dept. of Geology, Princeton, NJ, USA, 38 pp., avaiable at: ftp://ftp.whoi.edu/pub/users/cbowinnamedcopy_HHHess_1990_evolution_ocean_basins.pdf, 1960.

Hess, H. H.: History of Ocean Basins, in: Petrologic Studies: A Volume in Honor of A. F. Buddington, edited by: Engle, A. E. J., James, H. L., and Leonard, B. F., Boulder, CO, USA, Geological Society of America, 599–620, 1962.

Jekeli, C.: Alternative methods to smooth the earth's gravity field, project report, The Ohio State University, Ohio, USA, 1981.

Lerch, F. J., Klosko, S. M., Laubscher, R. E., and Wagner, C. A.: Gravity model improvement usig Geos 3 (GEM 9 and 10), J. Geophys. Res., 84, 3897–3916, 1976.

Marsh, J. G., Lerch, F. J., Putney, B. H., Felsentreger, T. L., Sanchez, B. V., Klosko, S. M., Patel, G. B., Robbins, J. W., Williamson, R. G., Engelis, T. L., Eddy, W. F., Chandler, N. L., Chinn, D. S., Kapoor, S., Rachlin, K. E., Braatz, L. E., and Pavlis, E. C.: The GEM-T2 gravitational model, J. Geophys. Res., 95, 22043–22071, 1990

Morgan, W. J.: Plate motions and deep mantle convection, Geol. Soc. Am. Mem., 123, 7–22, 1973.

Nerem, R. S., Bills, B. G., and McNamee, J. B.: A high resolution gravity model for Venus: GVM-1, Geophs. Res. Lett., 20, 599–602, 1993.

Pekeris, C. L.: Thermal convection in the interior of the Earth, Mon. Not. R. Astron. Soc., 3, 343–367, 1935.

Pellinen, L. P.: A method for expanding the gravity potential of the Earth in spherical harmonics, Translation ACIC-TC-1282, NTIS: AD-661819, Moscow, Russia, 1966.

Ricard, Y., Richards, M., Lithggow-Bertelloni, C., and Le Stuff, Y.: A geodynamical model of mantle density heterogeneity, J. Geophy. Res., 98, 21895–21909,1993.

Soloman, S. C. and Sleep, N.: Some simple physical models for absolute plate motions, J. Geophys. Res., 79, 2557–2564, 1974.

Smith, D., Lerch, F. J., Nerem, R. S., Zuber, M. T., Patel, G. B., Fricke, S. K., and Lemoine F. G.: An improved gravity model for Mars: Goddard Mars Model 1, J. Geophy. Res., 98, 20871–20889, 1993.

Vine, F. J. and Matthews, D. H.: Magnetic anomalies over oceanic ridges, Nature, 199, 947–940, 1963.

Wegener, A.: Die Entstehung der Kontinente, Geol. Rundsch., 3, 276–292, 1912 (in German).

Wilson, J. T.: A possible origin of the Hawaiian Islands, Can. J. Phys., 41, 863–870, 1963.

Wyrtki, K.: Fluctuations of the dynamic topography in the Pacific Ocean, J. Phys. Oceanogr., 5, 450–459. 1975.